

# Structural and angular dependence of coercivity and magnetic remanence of electrochemical ferromagnetic nanowires

A. Ghaddar<sup>1,\*</sup>, F. Gloaguen<sup>2</sup>, and J. Gieraltowski<sup>1</sup>

<sup>1</sup> *Laboratoire de Magnétisme de Bretagne, UBO,  
CNRS-FRE 3117, C. S. 93837 Brest Cedex 3, France*

<sup>2</sup> *Laboratoire de Chimie, Electrochimie Moléculaire et Chimie Analytique, UBO,  
CNRS-UMR 6521, C. S. 93837 Brest Cedex 3, France*

(Dated: October 31, 2018)

## Abstract

A novel method for controlling nanowire magnetic properties and growth from filling time profile is presented.

The wires are grown with an electrodeposition method ("Template synthesis") with a wide selection of pore diameters. We show that stray-fields presence in ferromagnetic nanowires are entirely dependent on the nanowire diameter. Besides a crossover effect in the reversal mechanism is observed with change in diameter. In this work, theory and experiment agree and confirm that according to the variety of hysteresis loop measured, about four ranges of values of pore diameter control the orientation of nanowire magnetization easy axis with respect to the geometrical axis.

PACS numbers: 75.75.+a, 75.60.Ch, 75.60.Jk, 62.23.Hj, 63.22.Gh

---

\*Electronic address: abbas.ghaddar@univ-brest.fr

## I. INTRODUCTION

There has been an increasing interest [1] in the fabrication and properties of nanostructured magnetic materials not only from a fundamental but also from a technological point of view, owing to their potential applications in magnetic recording media [2], biosensors and magnetic sensors based on the giant magneto-resistance effect [3, 4]. The ultimate density of recording media depends on the size of the individual magnetic elements. The miniaturization of the latter can now be realized through the electrodeposition of nanodots or nanowires into self-assembled arrays, such as track-etched polymer membranes and anodic alumina filters.

Structural and magnetic characterization of arrays of Nickel (Ni) nanowires produced by electrodeposition in polycarbonate membranes with diameters in the (15-100 nm) range and  $L = 6\mu\text{m}$  average length are made. The nanowires made within polycarbonate membranes, with various diameters (15 nm, 50 nm, 80 nm, 100 nm), are used to study the influence of the various parameters such as pore geometry and deposition process on the magnetic properties. Magnetization curves with various magnetic field orientations and nanowire diameters were determined at room temperature by magnetometry. According to the form of hysteresis loop measured, about four ranges of values of pore diameter control the orientation of easy axis of magnetization with respect to the wire axis. Reducing the diameter of the nanowires from 100 to 15 nm leads to increasing coercive fields from 347 to 590 Oe. The measured coercivity as a function of angle ( $\varphi$ ) between the field and wire axis reveals that the coercive field decreases (increases) with angle, peaking at  $\varphi = 0^\circ$ , for nanowire diameters smaller (larger) than 50nm.

”Template synthesis” is an elegant chemical approach to the manufacturing of nanostructured materials, in particular for different kinds of nanowires [5]. In this paper, arrays of Ni nanowires have been obtained by filling a porous polycarbonate membrane, which contains a large number of cylindrical holes with a narrow size distribution. Characterization and understanding of the magnetic properties of nanowire arrays have been a challenge for years. Some problems remain unclear. For example, there are still open questions about the mechanisms responsible for the magnetization reversal. The intrinsic properties of nanowire arrays are directly related to the properties of the nanoporous template such as the relative pore orientations in the assembly, pore size and its distribution, as well as interpore distance.

Two reversal modes have been suggested as being important: curling and coherent rotation. The critical diameter between coherent rotation and curling is  $d_c = 2\sqrt{\frac{A}{\pi} \frac{q}{M_S}}$ , ( $d_c$  is also called the coherent diameter),  $A = 1.5 \times 10^{-6}$  erg/cm is the exchange stiffness constant [6],  $M_S$  the saturation magnetization and  $q$  is a solution of a Bessel equation [7] (see section 3.1).

For wire diameter  $d < d_c$ , the Stoner-Wohlfarth coherent rotation model applies [8].

On the other hand for wire diameter  $d > d_c$ , the reversal occurs by inhomogenous reversal (curling). Increasing further the diameter until  $d \gg d_c$ , domains may form within the wire and the magnetization reversal, thus, may occur by domain wall motion [9].

As other extrinsic or hysteretic properties, coercivity (or coercive field)  $H_C$ , is strongly real-structure dependent. It is one of the most important properties of magnetic materials from the viewpoint of their technological utilization [10] and the understanding of its intrinsic mechanism is a permanent challenge. As different magnetization reversal mechanisms would give a different angular dependence of the coercivity  $H_C$ , the measurement of  $H_C(\varphi)$  would provide helpful information about the rotation mechanisms. Here,  $\varphi$  is defined as the angle between the field direction and the wire axis (Fig.1). For anisotropic, perfectly oriented polycrystalline magnets based on noninteracting particles, the coercive field  $H_C$  should be equal to the anisotropy field  $H_A$ . It is known [11], however, that the coercive field measured in permanent magnet materials is typically one order of magnitude lower than the anisotropy field. It is basically accepted that the origin of this discrepancy lies in the distribution of local alterations of the magnetic properties due to a variety of microstructural features giving rise to magnetization reversal through a process which includes a succession of mechanisms, as well as in the role played by interactions, either dipolar and/or exchange, during demagnetization.

Aside from coherent rotation, important coercivity mechanisms are, curling, localized nucleation, and domain-wall pinning. With increasing size, the nucleation mechanism in perfect ellipsoids of revolution changes from coherent rotation to curling. However, both coherent rotation and curling greatly overestimate the coercivity of most magnetic materials. Nucleation refers to the onset of magnetization reversal and determines the coercivity in nearly defect-free magnets.

Most works have concentrated on individual wires [12, 13], few [14, 15] reported on detailed measurements of  $H_C(\varphi)$  for nanowire arrays.

In this work, we set out to study the magnetic properties of various types of nanowires

possessing different diameters. Nanowires used in this work are fabricated in polycarbonate membranes, with various diameters (15 nm, 50 nm, 80 nm and 100 nm) in order to study the influence of the parameters such as pore shape and deposition process on the magnetic properties.

We infer from our study that basically four ranges of diameter values are important to determine the orientation of the easy axis with respect to the nanowire axis.

## II. EXPERIMENTAL

### A. Sample preparation

The nanowire samples are prepared by electrodeposition into the pores of nuclear-track-etched polycarbonate membranes PCTE (see Fig. 2) using an Autolab Potentiostat employing a three-electrode configuration and an electrolyte containing ion of the metals to be deposited [16].

During sputtering, a Copper layer was sputter-deposited on one side of the polycarbonate membrane and used as the working electrode to fabricate an array of Ni nanowires. A carbon plate and Ag/AgCl are used as the counter electrode and reference electrode, respectively. The work was carried out at a constant potential  $-1V$  (Ag/AgCl) at room temperature. The following aqueous electrolytes used was Nickel sulfate salt ( $NiSO_4 \cdot H_2O$ )(44g/l) in a boric acid solution ( $H_3BO_3$  )(40g/l). The latter was used as a buffer. The study of the magnetic properties of the wire demanded that deposition should stop when there is no covering of the upper surface of the membrane by a polluting layer of the magnetic material. During the deposition process, the time dependence of electrical current was monitored and recorded. Hence, the current intensity-time curve recorded during the electrodeposition process revealed four different regions (see Fig.3):

- Region I: coverage of the pore walls by the ions.
  
- Region II: filling of the pore interior by the growth.
  
- Region III: fast variation triggered by growth at the upper extremity of the pore and subsequent outgrowth beyond the pore. This occurs when the pores are completely filled

with the material, and the electrodeposited material begins to form hemispherical caps over the nanowire ends (see Fig. 4).

- Region IV is percolative growth outside the pores.

Attention has been focused on the region labeled II because it is always the most complicated to reproduce.

To understand the mechanism of growth materials in porous membrane, and to estimate the time of filling in the pores, a small comparative study between two electrodes was made. We took two Copper electrodes in the same area, which was stuck on the first porous membrane (electrode1). According to the nickel growth curves on two electrodes (current versus time), we can clearly see the difference between the two curves because on the first membrane electrode (electrode 1), the deposit is made on small surfaces while on the another takes place over the entire surface. After some time, the two curves intersect in a single point, which shows that the pores are filled by materials and it is time for the emergence of a film on the surface of the membrane (Region IV, Fig.3). This also indicates that deposition occurs on two equal surfaces (Fig. 5a).

Figure 5b shows an image of a sample in which all the nanowires are misaligned perpendicularly to the polycarbonate membrane plane. The majority of nickel nanowires tilt randomly a few degrees, with respect to the polycarbonate membrane plane normal.

## **B. Magnetization measurements**

The magnetic properties of the Ni nanowire array are studied by VSM (vibrating sample magnetometer), measurements which are performed at room temperature. The hysteresis loops at different angles between the magnetic field and the axis of the wires were measured.

Figure 6 shows four cases for the hysteresis loops with the external field  $H$ , perpendicular and parallel to the sample plane (i.e. parallel and perpendicular to the axis of the nanowires) for 4 samples with different diameters of (a) 15, (b) 50, (c) 80 and (d) 100 nm respectively.

The hysteresis loops and the coercivities change smoothly with the change in the applied field direction.

The saturation field, when the field is applied parallel to the axis of the nanowire, is

greater than that when the applied field is perpendicular to the nanowire for the 15 nm diameter sample. On the other hand we see the opposite case for 80 and 100 nm diameter samples. For the 50 nm sample the parallel and perpendicular saturation fields are equal. (See Fig. 6).

The coercivity dependence on the angles is shown in (Fig. 7a) demonstrating that coercivity decreases with the angle for nanowires that have 15 and 50 nm in diameter. In contrast, this is not the case of nanowires with 80 and 100 nm diameters.

FIG.7 (a-b) show the angular dependence of  $H_C(\varphi)$  and  $SQ(\varphi) = \frac{M_r}{M_S}$  (squareness) for Ni nanowire arrays in PCTE membranes, respectively.

However,  $H_C(\varphi)$  shows a quite different behavior for,  $d=15$  nm, 50 nm and  $d=80$  nm, 100 nm (Fig. 7a). For  $d=15$  nm and 50 nm, we observe a bell-type  $H_C(\varphi)$  variations, but for  $d=80$  nm and 100 nm a bowl shape  $H_C(\varphi)$  curve is observed.

These results imply that there is a crossover transition in magnetization reversal mechanisms for  $d \leq 50$  nm.

As shown in (Fig. 7b), for the two samples, 80 and 100 nm diameters, the squareness  $SQ(\varphi)$  of Ni nanowire array decreases with increase of angle, peaking at  $\varphi = 0^\circ$ , which is the easy axis of the arrays as can be seen from the magnetization curves (Fig. 6).

On the other hand, for the sample of 15 nm diameter the easy axis is perpendicular to the wire axis. For the 50 nm diameter sample, easy magnetization axis is off to an angle of  $30^\circ$  of the wire axis.

### III. THEORETICAL

In this work we can infer that single domain in the nanowires, and magnetization reversal modes can be modeled by homogeneous rotation when there is a critical size below which a particle remains in a single-domain state during switching, or inhomogeneous space dependent reversal  $\theta(r)$  when the particle size is larger then the critical size, but still in the single-domain regime. We assume that all our samples are in the single-domain regime [9].

### A. Magnetization in single-domain particles

In principle, the magnetization configuration in a magnetic nanowire can be determined from the Brown equations by minimizing the total free energy [17]. In bulk ferromagnetic materials, the energy of the system can be minimized by forming multiple magnetic domains within which the magnetic moments are aligned. However, there is a critical size below which a particle remains in a single-domain state during switching.

Approximating our single domain by an ellipsoid of revolution, the critical radius  $R_{sd}$  (minor axis,  $a = b$ ) for a single-domain particle can be expressed [17], and calculated by comparing the exchange energy averaged over the ellipsoid volume to the magnetostatic energy; [Appendix A]. One finds:

$$R_{sd} = \sqrt{\frac{6A}{N_C M_S^2} \left[ \ln\left(\frac{4R_{sd}}{a_1}\right) - 1 \right]}$$

Where  $N_C$  is the demagnetization factor along the c axis (Fig. 1) and  $a_1$  is the nearest-neighbor spacing. The critical radius for a single-domain particle is dependent on the material parameters  $A, a_1, M_S$ .

If we consider the infinite cylinder case ( $R_{sd} \rightarrow \infty, N_C \rightarrow 0$ ), in the single domain case there is a critical size between the two magnetization reversal processes. When the magnetic easy axis is aligned with the applied field, the critical radius  $r_c = \frac{dc}{2}$  for the transition between coherent and curling effect is defined by [7]:

$$r_c = \sqrt{\frac{2A}{N_a} \frac{q}{M_s}}$$

where  $q = 1.8412$  for a cylinder is the first maximum of the Bessel equation  $\frac{d}{dx}(J_1(q)) = 0$ , where  $J_1(q)$  is the ordinary Bessel's function of the first kind and  $N_a = 2\pi$  is the demagnetizing factor along the minor axis of the infinitely long cylinder. Hence:

$$r_c = \sqrt{\frac{A}{\pi} \frac{q}{M_S}}$$

Coherent and curling model rotation are illustrated in Fig.8

For the theoretical explanation of these two magnetization modes, we consider the elongated single-domain particle with uniaxial anisotropy shown in Fig.1.

## B. Coherent rotation

In the Stoner-Wohlfarth (SW) coherent rotation model [18], the total free energy consists of the crystalline and shape anisotropy and Zeeman energy due to the external magnetic field.

$$E = K \sin^2 \theta - M_S H \cos(\theta - \varphi), \quad (1)$$

Where  $(\theta)$  is the angle between the  $M_S$  and the easy axis,  $K$  is the effective anisotropy,  $(\varphi)$  is the angle between the external applied field and the easy direction;  $(\theta - \varphi)$  is the angle between  $M_S$  and  $H$ .

$$K = \frac{M_S^2}{2}(N_a - N_C) + K_1$$

Here  $N_a$  and  $N_C$  are the demagnetizing factor of the ellipsoid along the minor and the long axis respectively, and  $K_1$  is the magnetocrystalline anisotropy constant,  $K_1$  is small by comparing with  $\frac{M_S^2}{2}(N_a - N_C)$ .

After using  $\frac{\partial E}{\partial \theta} = 0$  and  $\frac{\partial^2 E}{\partial \theta^2} = 0$  we obtain:

$$H_S = \frac{H_K}{[\sin^2 \varphi^{\frac{2}{3}} + \cos^2 \varphi^{\frac{2}{3}}]^{\frac{3}{2}}}$$

where  $H_S$  is the switching field and  $H_K$  is the effective anisotropy field :  $H_K = \frac{2K}{M_S}$ .

(The detailed calculation is in appendix B).

On the other hand, the coherent rotation mode [17] gives the highest and the lowest coercivity field  $H_C(\varphi)$  value of  $H$  parallel and perpendicular to the easy axis, respectively, for the 15 and 50 nm of diameter.

In the Stoner-Wohlfarth model the switching field ( $H_S$ ), does not represent the coercivity,  $H_C(\varphi)$ , in all cases. However, from the discussion in [18], the coercivity can be written as

$$H_C = \begin{cases} H_{C1} \\ H_{C2} \end{cases} \text{ for } \begin{cases} 0 \leq \varphi \leq \pi/4, \\ \pi/4 \leq \varphi \leq \pi/2, \end{cases} \quad (2)$$

with

$$H_{C1} = |H_S| = \frac{2K}{M_S} \frac{1}{[\sin^2 \varphi^{\frac{2}{3}} + \cos^2 \varphi^{\frac{2}{3}}]^{\frac{3}{2}}}$$



$$H_{C2} = 2 \left| H_S(\varphi = \frac{\pi}{4}) \right| - \left| H_S(\frac{\pi}{4} \leq \varphi \leq \frac{\pi}{2}) \right|.$$

In this mode, two regimes can be identified, when the applied field is close to the magnetic easy axis,  $0^\circ \leq \varphi \leq 45^\circ$ , the hysteresis loop is relatively square; hence, the change in sign of the magnetization, corresponding to the coercivity, occurs at the switching field.

In this regime the coercivity field  $H_{C1}$  is equal to the switching field  $H_S$ .

For  $45^\circ \leq \varphi \leq 90^\circ$ , the applied field is oriented closer to the magnetic hard axis, and the hysteresis loop is sheared such that switching occurs after the magnetization changes sign. In this case,  $H_C \neq H_S$  and the coercive field is determined from equation ( $H_{C2}$ ).

### C. Curling

The magnetization curling mode was defined by Frei et al [17] and after it has been used for different structures to investigate the magnetic switching of films [19], spherical particles, prolate ellipsoids [17] and cylinders [20]. For particle size larger than the critical size but still in the single-domain regime, magnetization reversal occurs by curling [17, 19]. In the curling model, magnetization switching is an abrupt process, and the switching field is very close to the nucleation field; hence,  $H_C = H_S$  for all angles.

The curling nucleation field is given by [21].

$$h \cos(\varphi - \theta) = \frac{1}{2\pi}(N_a \sin^2 \theta + N_C \cos^2 \theta) - \frac{k}{S^2}, \quad (3)$$

where  $S$  is the reduced radius defined as  $R/R_0$ ,  $R$  is the radius of the cylinder and  $R_0$  is the exchange length defined by  $R_0 = \frac{\sqrt{A}}{M_S}$ , and  $R_0 = 25.2$  nm for Ni. Here  $h = \frac{H}{2\pi M_S}$  is the reduced field [20] and the parameter  $k = 1.08$ , which is  $q^2/\pi$  in the notation of Ref. [7], is a monotonically decreasing function of the aspect ratio  $m = \frac{c}{a}$  of the ellipsoid (Fig. 1).

To complete the calculation it is still necessary to eliminate the angle  $\theta$  from **(3)**.

By using the fact that it is the same angle as in:

$$h \sin(\varphi - \theta) = \frac{1}{2\pi}(N_a - N_C) \sin 2\theta \quad (4)$$

it will become after the differentiating  $E$  with respect to  $\theta$ .

$$\frac{\partial E}{\partial \theta} = 2K \sin \theta \cos \theta + M_S H \sin(\theta - \varphi) = 0.$$

One way of doing it to consider Eqs (3) and (4) as two linear equations in  $h \sin \varphi$  and  $h \cos \varphi$  and to solve them as such obtaining:

$$\begin{aligned} h \sin \varphi &= \left( \frac{1}{2\pi} N_a - \frac{k}{S^2} \right) \sin \theta \\ h \cos \varphi &= \left( \frac{1}{2\pi} N_C - \frac{k}{S^2} \right) \cos \theta \end{aligned} \quad (5)$$

Adding the squares of these equations by using:

$$\cos^2 \theta + \sin^2 \theta = 1$$

leads to

$$h_S = \frac{\left( \frac{N_C}{2\pi} - \frac{k}{S^2} \right) \left( \frac{N_a}{2\pi} - \frac{k}{S^2} \right)}{\sqrt{\left( \frac{N_C}{2\pi} - \frac{k}{S^2} \right)^2 \sin^2 \varphi + \left( \frac{N_a}{2\pi} - \frac{k}{S^2} \right)^2 \cos^2 \varphi}}$$

where  $h_S = \frac{H_S}{2\pi M_S}$ .

For the infinite cylinder,  $N_C = 0$ ,  $N_a = 2\pi$ , and  $k = 1.08$  we obtain

$$h_S = h_C = \frac{1.08(1 - 1.08S^{-2})}{S^2[1.1664S^{-4} + \cos^2 \varphi(1 - 2.16S^{-2})]^{\frac{1}{2}}}.$$

The coercivities of infinite cylinders with shape anisotropy depends only on the value of  $S$  and the angle  $\varphi$  between the easy axis of magnetization and the direction of measurement as shown in (Fig. 9-10) and plotted in reduced units  $h_c(\varphi)$  ( $0 < h_c < 1$ ) for various values of  $S$ .  $H_C$  versus  $\varphi$  curves are illustrated in Fig. 11. When we compare the curves in Fig. 7a and Fig. 11, the coherent magnetization reversal is for the 15 nm and 50 nm of diameters and the curling mode is for the 80 nm and 100 nm of diameters.

In order to observe small variation in the coercivity, very well geometrically characterized samples need to be measured with well controlled inter-wire interaction. In our samples the center to center distance is fixed, and the strength of interactions is different from sample to sample, making direct comparison difficult. The fitted values for the coercivity are larger than the experimental data and  $H_C(\varphi)$  values are actually much smaller than  $2\pi M_S = 3050$  Oe, which is expected for an individual wire.

We ascribe such differences between calculations and experimental results to the interaction of each wire with the stray field produced by the array. This field originating from the effective ferromagnetic coupling between neighboring wires reduces the coercive field [22, 23].

Fig. 6 a, shows there is a flat behaviour in the  $H_C(\varphi)$  curve at low angles for 80 and 100 nm of diameters, which may be caused by the variation of wire orientation with respect to the normal to the membrane plane.

These results suggest that the interwire coupling cannot be neglected even for PCTE membranes.

#### IV. DISCUSSION

In the case of a single domain wire, we have to consider three different field acting on the wire [24]:

$$H_{eff} = H_{Sh} + H_A + H_D$$

where  $H_{Sh}$  is the demagnetization field (shape),  $H_A$  is the effective anisotropy field and  $H_D$  is the average dipolar field between the wires.

The demagnetization field (shape)  $H_{Sh}$  of the individual wire if magnetized parallel to the pore axis is of the order of  $2\pi M_S = 3050$  Oe with  $M_S$  equal to  $485$  emu/cm<sup>3</sup>.

The effective anisotropy field  $H_A$ , given by  $H_A = -\frac{4}{3}\frac{K_1}{M_S} = 123$  Oe with  $K_1 = -4.5 \times 10^4$  erg/cm<sup>3</sup> is the cubic magnetocrystalline anisotropy [25] of Ni.

The in plane average dipolar field between the wires, which tends to induce a magnetic easy axis perpendicular to the wire axis.

For a qualitative analysis, we consider a two-dimensional infinite array of magnetic dipoles. The array is formed by a square dipole mesh of size  $D$ . When we assume all the moments are aligned along the wires, the average dipolar field, which acts on each wire, is parallel to the axis of the wire and may be expressed as [26, 27]:

$$H_{D_0} = [4.2M_S(\pi d^2/4)L]/D^3 \quad (6)$$

On the other hand, for the same array with magnetic moments aligned perpendicularly to the axes of the wires, the average dipolar field which acts on every wire may be expressed as [26, 27]:

$$H_{D_{90}} = [-2.1M_S(\pi d^2/4)L]/D^3 \quad (7)$$

where  $d$  is the diameter of the wire,  $L$  is the length, and  $D$  is the inter-wire distance [Appendix C].

While the total effective fields following the two directions parallel ( $0^\circ$ ) and perpendicular ( $90^\circ$ ) to the wire axis may be written:

$$H_{eff}(total) = \begin{cases} (0^\circ) \rightarrow H_{D_0} + H_A \\ (90^\circ) \rightarrow H_{D_{90}} + H_{Sh} \end{cases}$$

The calculation for the various angles, show that  $H_C(\varphi)$  decreases as the angle increases, with a bell-type variation. Therefore, the magnetization reversal was determined mainly by the curling mode, as shown in (Fig. 6a) for 80 nm and 100 nm diameters. For Ni nanowires, the curling is predicted for  $d \geq 50$  nm, this value agrees with prior work on ordered Ni nanowire arrays in alumina [28] where the critical diameter was 40 nm. The coherent rotation will occur for 15 and 50 nm wires, which is consistent with results in (Fig. 6a). In the same way, the squareness  $SQ(\varphi)$  of hysteresis loops is measured for different orientations of wires as a function of the applied magnetic field. It can be seen that for large wire diameters the maximum  $SQ(\varphi)$  is found when the magnetic field is applied parallel to the axis of the wire and the minimum occurs when the applied field is perpendicular to the axis of the wire (see Fig. 6.b). This concurs with the abovementioned idea that for the larger wire diameters, the easy axis of magnetization is parallel to the axis of the wires. On the other hand, for the 50 nm of diameters of wires (see Fig. 6.b), the behavior of  $SQ(\varphi)$  indicates that we are in the crossover region where the axes begin to rotate from parallel to perpendicular to the wire axis. But in the wires of 15 nm of diameter, the behavior of  $SQ(\varphi)$  indicates that we are in the perpendicular to the axes of the wires becomes the dominant easy axis of effective anisotropy.

## V. CONCLUSION

In conclusion, by means of theoretical studies and experimental measurements, we have investigated the reversal processes in ferromagnetic nanowires. Our systematic studies of

the effect of the nanowire size diameter show that the magnetization reversal mechanism is strongly influenced by the diameter value of the nanowires. The various types of  $H_C(\varphi)$  curves observed in (Fig. 7) suggest that no simple magnetization reversal mode could account for the complex coercivity mechanism. Two reversal modes are considered as the most important: coherent rotation and curling. Good agreement between the measured magnetic properties of Ni nanowires and the theoretical calculations is obtained. However, further experimental work remains to be done in order to observe this transition.

### Acknowledgments:

The authors wish to acknowledge Prof. C. Tannous (LMB) for his valuable discussions and help.

## VI. APPENDIX A

### Critical radius $R_{sd}$ for single domain

We consider in Fig. 1,  $a = b = R$  as the short axis, and  $c$  as the long axis of the ellipsoid

$$E_X = A\left[\left(\frac{d\theta}{dr}\right)^2 + \frac{1}{r^2} \sin^2 \theta\right]$$

Approximating:  $\theta(r) \rightarrow \frac{\pi}{2}$  The average over ellipsoid:

$$\bar{E}_X = \frac{1}{\frac{4}{3}\pi R^2 c} \int \frac{A}{r^2} 2\pi r dr dZ$$

with equation:  $\frac{r^2}{R^2} + \frac{Z^2}{c^2} = 1 \Rightarrow Z = \pm c\sqrt{1 - \frac{r^2}{R^2}}$

$$\Rightarrow \bar{E}_X = \frac{1}{\frac{4}{3}\pi R^2 c} \int_{a_{1/2}}^R 2\pi A \frac{dr}{r} \int_0^{c\sqrt{(1-\frac{r^2}{R^2})}} 2dZ$$

where  $a_1$  is the nearest-neighbor spacing

$$\Rightarrow \bar{E}_X = \frac{3A}{R^2 c} \int_{a_{1/2}}^R \frac{dr}{r} \int_0^{c\sqrt{(1-\frac{r^2}{R^2})}} dZ$$

$$\Rightarrow \bar{E}_X = \frac{3A}{R^2 c} \int_{a_{1/2}}^R \frac{dr}{r} c \sqrt{1 - \frac{r^2}{R^2}}$$

changing:  $\frac{r}{R} = \cos x \Rightarrow \frac{dr}{R} = -\sin x dx$

$$\Rightarrow \bar{E}_X = \frac{3A}{R^2} \int_0^{\arccos(a_{1/2}/2R)} \frac{R \sin^2 x}{R \cos x} dx$$

$$\Rightarrow \bar{E}_X = \frac{3A}{R^2} \int_0^{\arccos(a_{1/2}/2R)} \frac{\sin^2 x}{\cos x} dx$$

From the integral:  $\int \frac{\sin^2 x}{\cos x} dx = -[\sin x + \ln \operatorname{tg}(\frac{\pi}{4} - \frac{x}{2})]$

Taking:  $u = \arccos(a_{1/2}/2R) \Rightarrow a_{1/2}/2R = \cos u$

$$\Rightarrow \bar{E}_X = -\frac{3A}{R^2} [\sin u + \ln \operatorname{tg}(\frac{\pi}{4} - \frac{u}{2})]$$

using:  $B = \ln \operatorname{tg}(\frac{\pi}{4} - \frac{u}{2}) = \ln \left[ \frac{\cos \frac{u}{2} - \sin \frac{u}{2}}{\cos \frac{u}{2} + \sin \frac{u}{2}} \right]$

with  $t = \operatorname{tg} \frac{u}{2}$ ,  $B = \frac{1-t}{1+t} = \frac{(1-t)^2}{1-t^2} = \frac{1+t^2-2t}{1-t^2}$

$$\Rightarrow B = \frac{1}{\cos u} - \operatorname{tg} u = \frac{1 - \sin u}{\cos u} = \frac{1 - \sqrt{1 - (\frac{a_1}{2R})^2}}{\frac{a_1}{2R}}$$

$$\Rightarrow B = \frac{1 - (1 - \frac{1}{2}(\frac{a_1}{2R})^2 \dots)}{\frac{a_1}{2R}}, \Rightarrow B \cong \frac{a_1}{4R}$$

$$\Rightarrow \bar{E}_X = -\frac{3A}{R^2} \left[ 1 + \ln \frac{a_1}{4R} \right] = \frac{3A}{R^2} \left[ \ln \frac{4R}{a_1} - 1 \right]$$

Comparing this energy to the magnetostatic energy:

We get:  $E_D = \frac{1}{2} M_S^2 N_c$

$$\Rightarrow R_{sd} = \sqrt{\frac{6A}{N_C M_S^2} \left[ \ln \left( \frac{4R_{sd}}{a_1} \right) - 1 \right]}$$

## VII. APPENDIX B

### Stoner-Wohlfarth (SW) coherent rotation model

The total free energy, (see Fig. 1)

$$E = K \sin^2 \theta - M_S H \cos(\theta - \varphi)$$

After differentiating  $E$  with respect to  $\theta$ , we obtain

$$\frac{\partial E}{\partial \theta} = 2K \sin \theta \cos \theta + M_S H \sin(\theta - \varphi),$$

We find that for a minimum in  $E$ ,  $\frac{\partial E}{\partial \theta} = 0$ , i. e;

$$2K \sin \theta \cos \theta + H M_S \sin(\theta - \varphi) = 0$$

After using the trigonometry equation:

$\sin(\theta - \varphi) = \sin \theta \cos \varphi - \cos \theta \sin \varphi$  We find:

$$\left[ 2K + \frac{H M_S \cos \varphi}{\cos \theta} - \frac{H M_S \sin \varphi}{\sin \theta} \right] \sin \theta \cos \theta = 0$$

Substituting:  
 $H_Z = H \cos \varphi$   
 $H_X = H \sin \varphi$

If we exlude the extrema at  $\theta = 0, \pi$  and  $\theta = \frac{\pi}{2}, \frac{3\pi}{2}$ , we can assume that above terms (in square brackets) is zero.

$$2K + \frac{H_Z M_S}{\cos \theta} - \frac{H_X M_S}{\sin \theta} = 0$$

Defining:  
 $h_z = \frac{H_Z M_S}{2K} = \frac{H_Z}{H_K}$ ,  $H_K = \frac{2K}{M_S}$   
 $h_x = \frac{H_X M_S}{2K} = \frac{H_X}{H_K}$

The second derivation gives:

$$\frac{\partial^2 E}{\partial \theta^2} = \frac{h_x \sin \theta}{\cos^2 \theta} + \frac{h_z \cos \theta}{\sin^2 \theta}$$

After using  $\frac{\partial E}{\partial \theta} = 0$  and  $\frac{\partial^2 E}{\partial \theta^2} = 0$ , we obtain:

$$\frac{h_x}{\cos \theta} - \frac{h_z}{\sin \theta} = 1 \quad (B.1)$$

$$\frac{h_z}{\sin^3 \theta} = -\frac{h_x}{\cos^3 \theta} \quad (B.2)$$

Eliminating  $\theta$  from these equation we obtain:

By (B.2),  $h_x = -\frac{\sin^3 \theta}{\cos^3 \theta} h_z$

Trough (B.1),  $-\frac{\sin^2 \theta}{\cos^3 \theta} h_z - \frac{h_z}{\cos \theta} = 1$

Factorizing:  $\frac{-1}{\cos^3 \theta} [\sin^2 \theta + \cos^2 \theta] h_z = 1$

We get 
$$\begin{cases} h_z = -\cos^3 \theta \\ h_x = \sin^3 \theta \end{cases},$$

which gives us  $h_x^{2/3} + h_z^{2/3} = 1$ , (Astroid equation)

Replacing  $h_x$  and  $h_z$  by these values we find the switching field  $H_S$  :

$$H_S = \frac{H_K}{[\sin \varphi^{2/3} + \cos \varphi^{2/3}]^{3/2}}$$

## VIII. APPENDIX C

### Dipolar interaction field

If we have a single dipole  $\vec{P}_0$  surrounded by an array of dipoles  $\vec{P}_i$  (Fig. C1), the interaction is:

$$E = \sum_i \frac{\vec{P}_0 \cdot \vec{P}_i}{r^3} - \frac{3(\vec{P}_0 \cdot \vec{r})(\vec{P}_i \cdot \vec{r})}{r^5}$$

This is equivalent to a field  $H_D$  acting on the dipole such that:  $E = -\vec{P}_0 \cdot \vec{H}_D$

$$\Rightarrow -\vec{P}_0 \cdot \vec{H}_D = \sum_i \frac{\vec{P}_0 \cdot \vec{P}_i}{r^3} - \frac{3(\vec{P}_0 \cdot \vec{r})(\vec{P}_i \cdot \vec{r})}{r^5}$$

### Calculating $H_{Dz}$

Assuming the dipoles  $\vec{P}_i$  sit on a 2D square lattice of parameter  $D$  (the average nanowire separation)

$|\vec{P}_0| = 1$ , is directed along the  $Z$  axis,

hence  $\vec{P}_0 = \begin{bmatrix} 0 \\ 0 \\ 1 \end{bmatrix} \Rightarrow -\vec{P}_0 \cdot \vec{H}_D = -H_{Dz}$

and  $\vec{P}_i = \begin{bmatrix} P_x \\ P_y \\ P_z \end{bmatrix}$ , and  $\vec{r} = \begin{bmatrix} iD \\ jD \\ 0 \end{bmatrix} \Rightarrow \vec{P}_0 \cdot \vec{r} = 0, \vec{P}_i \cdot \vec{P}_0 = P_z$ ,

we have  $r^3 = D^3(i^2 + j^2)^{3/2}$

Then,  $H_{Dz} = -\sum \frac{P_z}{r^3}$

$P_z = M_S V$  (All surrounded dipoles saturated along  $Z$ ):



$$\Rightarrow H_{Dz} = -\frac{M_S V}{D^3} \sum_{i,j} \frac{1}{(i^2 + j^2)^{3/2}}$$

$$\sum_{\substack{i,j = -\infty \\ (i,j \neq 0)}}^{+\infty} \frac{1}{(i^2 + j^2)^{3/2}} = 4 \sum_{\substack{i = 1, \infty \\ j = 1, \infty}} \frac{1}{(i^2 + j^2)^{3/2}}$$

Numerically:

$$4 \sum_{\substack{i = 1, \infty \\ j = 1, \infty}} \frac{1}{(i^2 + j^2)^{3/2}} = 4 \sum_{\substack{i = 1, 100 \\ j = 1, 100}} \frac{1}{(i^2 + j^2)^{3/2}} \cong 4 \times (1.05)$$

$$\Rightarrow H_{Dz} = \frac{-4.2 M_S V}{D^3}$$

**Calculating  $H_{Dx}$  :**

Taking,

$$\vec{P}_0 = \begin{bmatrix} 1 \\ 0 \\ 0 \end{bmatrix}, \vec{P} = \begin{bmatrix} P_X \\ P_Y \\ P_Z \end{bmatrix}, \text{ and } \vec{r} = \begin{bmatrix} iD \\ jD \\ 0 \end{bmatrix},$$

$$\Rightarrow E = -\vec{P}_0 \cdot \vec{H}_D = -H_{Dx}, \vec{P}_0 \cdot \vec{P} = P_X$$

$$\Rightarrow E = \sum_i \frac{P_X}{r^3} - \frac{3(iD)(P_X iD + P_Y jD)}{r^5}$$

We get  $E = \sum_i \frac{r^2 P_X - 3D^2(i^2 P_X + ij P_Y)}{r^5}$

$$\Rightarrow H_{Dx} = - \sum_{i,j=-\infty}^{+\infty} \frac{P_X(i^2 + j^2) - 3(i^2 P_X + ij P_Y)}{D^3(i^2 + j^2)^{5/2}}$$

If all the surrounding dipoles are saturated along X:

$$\Rightarrow P_X = M_S V, P_Y = 0$$

we get  $H_{D_x} = \frac{M_S V}{D^3} \sum_{i,j=-\infty}^{\infty} \frac{(2i^2-j^2)}{(i^2+j^2)^{5/2}} \Rightarrow H_{D_x} = \frac{4M_S V}{D^3} \sum_{i,j=1}^{\infty} \frac{(2i^2-j^2)}{(i^2+j^2)^{5/2}}$

Numerically:

$$\sum_{i,j=1}^{\infty} \frac{(2i^2-j^2)}{(i^2+j^2)^{5/2}} \cong \sum_{i,j=1}^{100} \frac{(2i^2-j^2)}{(i^2+j^2)^{5/2}} \cong 0.526$$

$$\Rightarrow H_{D_x} = 4(0.526) \frac{M_S V}{D^3} = 2.1 \frac{M_S V}{D^3}$$

$$\Rightarrow H_{D_x} = -\frac{1}{2} H_{D_z}$$

This shows the dipolar field along x is half the field along Z.

- 
- [1] M. Zheng et al., Phys. Rev. B, **62**, 12282 (2000).
  - [2] S. Manalis et al., Appl. Phys. Lett. **66**, 2585 (1995).
  - [3] Yoshida, M. et al., J. Radiation Effects in solids **126**, 409 (1993).
  - [4] Piraux, L. et al., Appl. Phys. Lett. **65**, 2484 (1994).
  - [5] C. J. Brumlik and C. R. Martin, Analytical Chem. **59**, 2625 (1992).
  - [6] G. Bertotti, *"Hysteresis in magnetism"*, Academic Press, New-York (1998).
  - [7] A. Aharoni, *"Introduction to the theory of ferromagnetism"*, Oxford University Press, New York, (1996).
  - [8] E. C. Stoner and E. P. Wohlfarth, Philos. Trans. R. Soc. London, Ser. A **240**, 599 (1957).
  - [9] R. Skomski, A. Kashyap, K. D. Sorge, D. J. Sellmyer J. Appl. Phys. **95**, 7022 (2005).
  - [10] H. Kronmüller, Phys. Status Solidi B **144**, 385 (1987).
  - [11] M. Sagawa, S. Fujimura, N. Tagawa, and Y. Matsuura, J. Appl. Phys. **55**, 2083 (1992).
  - [12] M. Lederman, R. O'Barr, and S. Schultz, IEEE Trans. Magn. **31**, 3793 (1995); R. O'Barr, M. Lederman, S. Schultz, W. H. Xu, A. Scherer, and J. Tonucci, J. Appl. Phys. **79**, 5303 (1996).
  - [13] W. Wernsdorfer, B. Doudin, D. Mailly, K. Hasselbach, A. Benoit, J. Meier, J.-Ph. Ansermet, and B. Barbara, Phys. Rev. Lett. **77**, 1873 (1996).
  - [14] A. K. M. Bantu, J. Rivas, G. Zaragoza, M. A. Lopez-Quintela, and M. C. Blanco, J. Appl. Phys. **89**, 3393 (2001).

- [15] J. M. Garcia, A. Asenjo, J. Velazquez, D. Garcia, M. Vazquez, P. Aranda, and E. Ruiz-Hitzky, *J. Appl. Phys.* **85**, 5480 (1999).
- [16] T. M. Whitney, J. S. Jiang, P. C. Searson, and C. L. Chien, *Science* **261**, 1316 (1993).
- [17] E.H. Frei, S. Shtrikman, and D. Treves, *Phys. Rev.* **106**, 446 (1957).
- [18] E. C. Stoner and E. P. Wohlfarth, *Phil. Trans. Roy. Soc. Lond. A* **240**, 599 (1948). Reprinted in *IEEE Trans. Magn.* **27**, 3475 (1991)
- [19] Y. Ishii, S. Hasegawa, M. Saito, Y. Tabayashi, Y. Kasajima, and T. Hashimoto, *J. Appl. Phys.* **82**, 3593 (1997).
- [20] Y. Ishii, M. Sato, *J. Appl. Phys.* **65**, 3146 (1989).
- [21] A. Aharoni, *J. Appl. Phys.* **82**, 1281 (1997).
- [22] R. Hertel, *J. Appl. Phys.* **90**, 5752 (2001).
- [23] M. Bahiana, F. S. Amaral, S. Allende, and D. Altbir, *Phys. Rev. B.* **74**, 174412 (2006).
- [24] G. C. Han, *IEEE Trans. Magn.* **38**, No. 5, 2562 (2002).
- [25] S. Chikazumi *"Physics of Ferromagnetism"*, Wiley, New York (1964).
- [26] G. J. Strijkers, J. H. J. Dalderop, M. A. Abroeksteeg, H. J. M. Swagten, and W. J. M. de Jonge, *J. Appl. Phys.*, **86**, 5141 (1999).
- [27] J. Jackson, *"Classical Electrodynamics"*, Wiley, New York (1962).
- [28] K. Neilsch, R. B. Wehrspohn, J. Barthel, J. Kirschner, U. Gl"osele *Appl. Phys. Lett.* **79**, 9, 1360 (2001).

## Figures

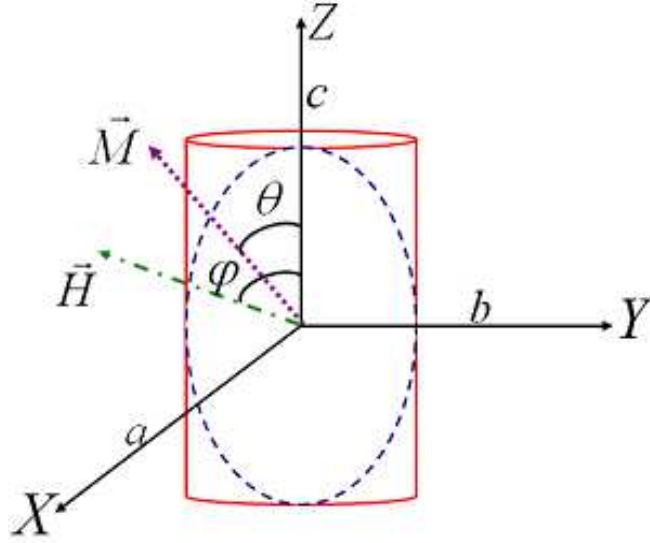


FIG. 1: Single domain particle with uniaxial anisotropy in presence of applied field  $H$ , showing angles,  $\theta$  and  $\varphi$  that  $\vec{M}$  and  $\vec{H}$  make with wire axis along  $Z$ , ( $a = b < c$ ).

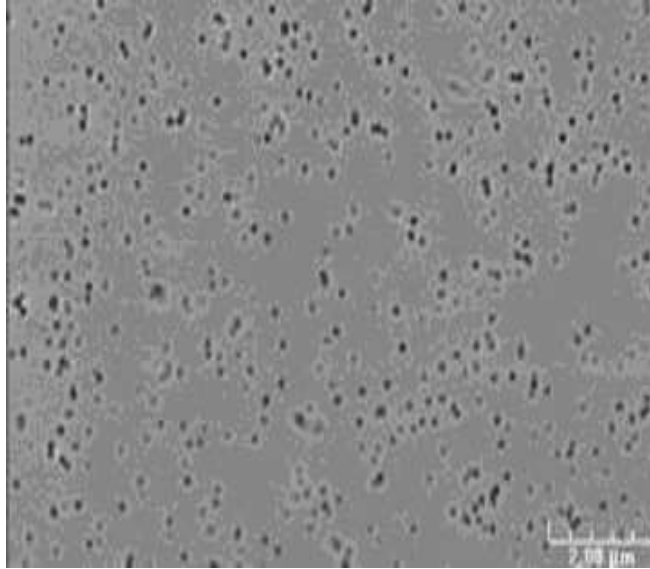


FIG. 2: Polycarbonate PCTE membrane with 80 nm pore diameter.

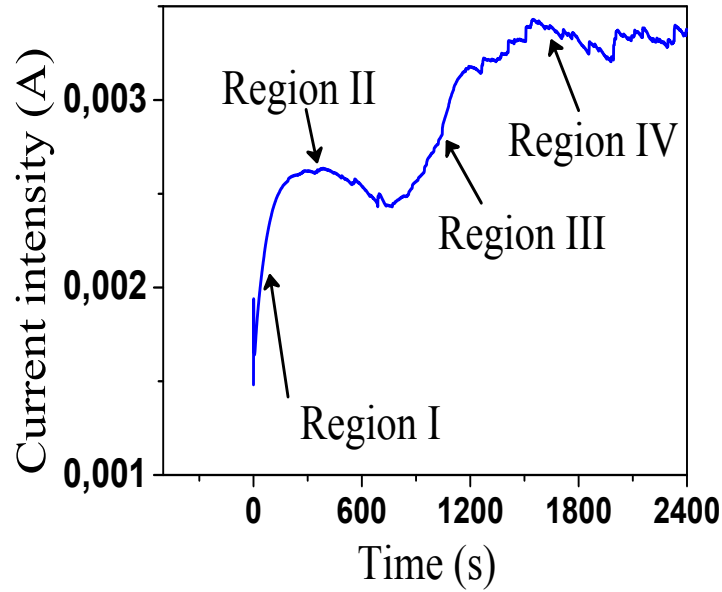


FIG. 3: Typical time variation of cathode current during electrodeposition of Ni nanowires arrays or we see the four regions, coverage of the pore walls by the ions (region I), filling of the pore interior by the growth (region II), fast variation triggered by growth at the upper extremity of the pore and subsequent outgrowth beyond the pore. This occurs when the pores are completely filled with the material, and the electrodeposited material begins to form hemispherical caps over the nanowire ends (region III), percolative growth outside the pores (region IV).



FIG. 4: SEM observation of the top surface where the Ni nanowires emerge from the polycarbonate PCTE membranepores in region III.



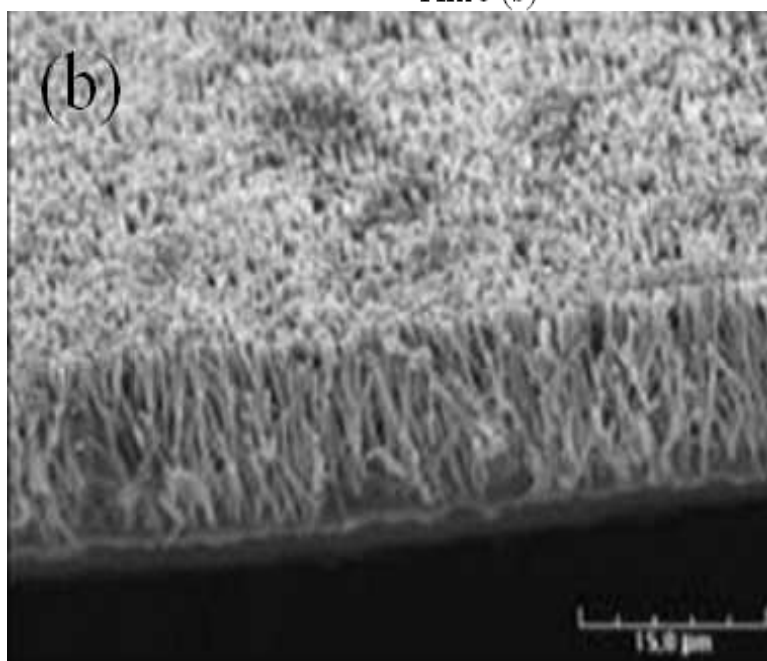
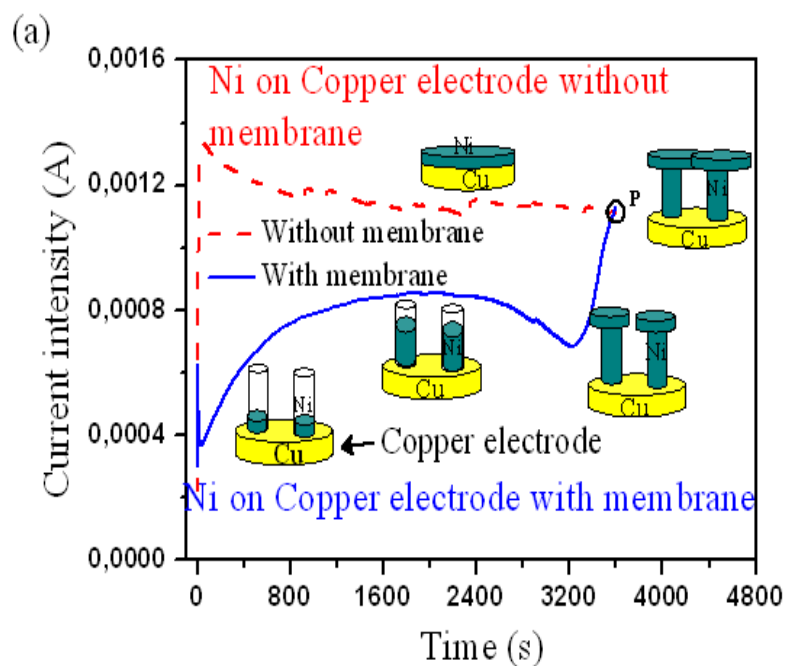
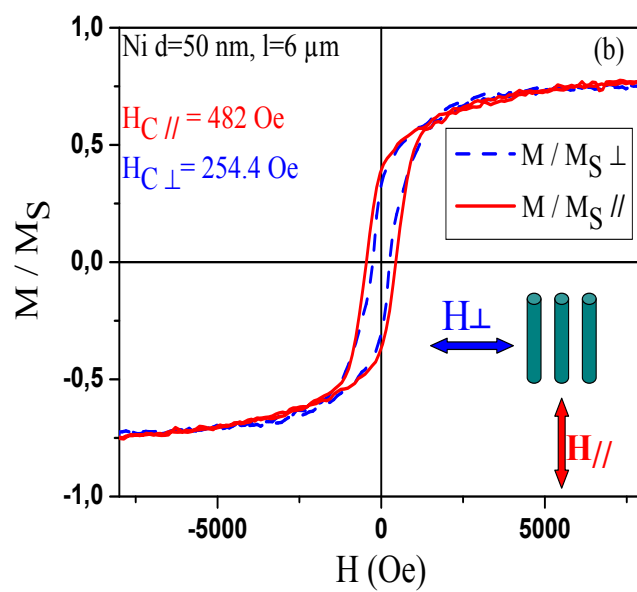
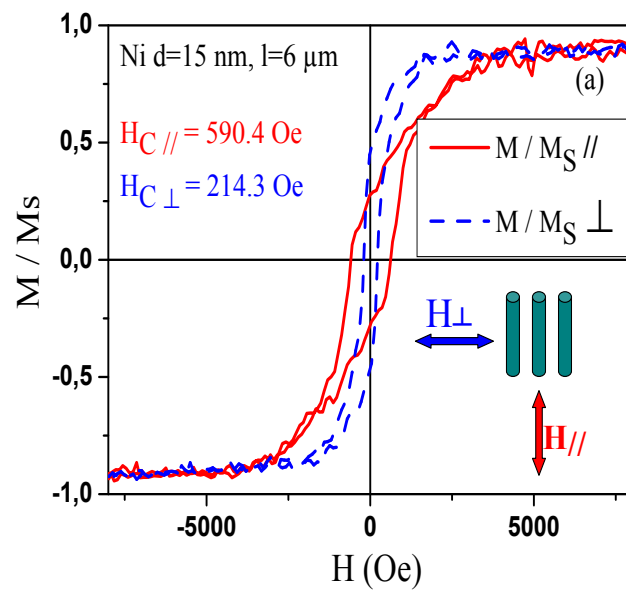


FIG. 5: Time variation of cathodic current during electrodeposition of Ni nanowires arrays when we can determine the exact time of filling of the pores (a) the two intensity curves cut at point P where the values of the top surfaces are the same. SEM image of a sample in which all the nanowires are misaligned perpendicular to the polycarbonate membrane plane (b).



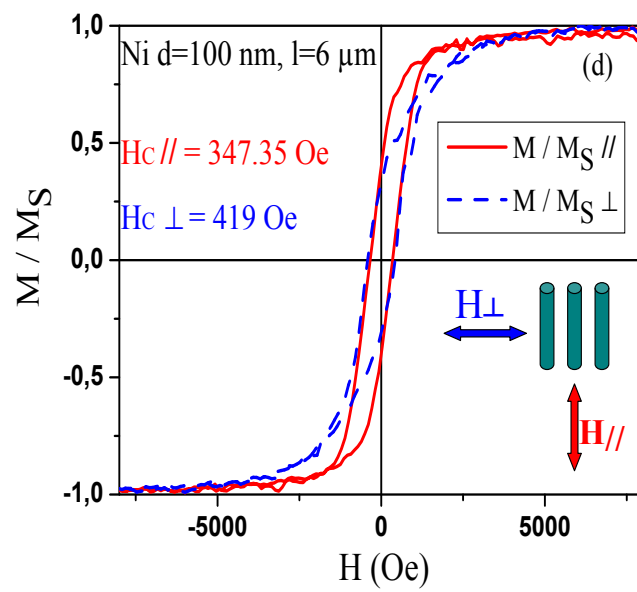
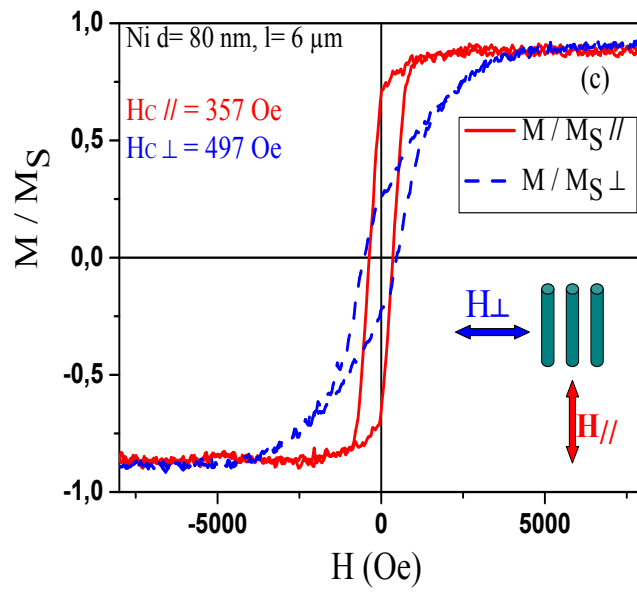


FIG. 6: a- The hysteresis loops when the external field is perpendicular and parallel to the axis wires for 15 nm and  $6\mu\text{m}$  length.

b- The hysteresis loops when the external field is perpendicular and parallel to the axis wires for 50 nm and  $6\mu\text{m}$  length.

c- The hysteresis loops when the external field is perpendicular and parallel to the axis wires for 80 nm and  $6\mu\text{m}$  length.

d- The hysteresis loops when the external field is perpendicular and parallel to the axis wires for 100 nm and  $6\mu\text{m}$  length.

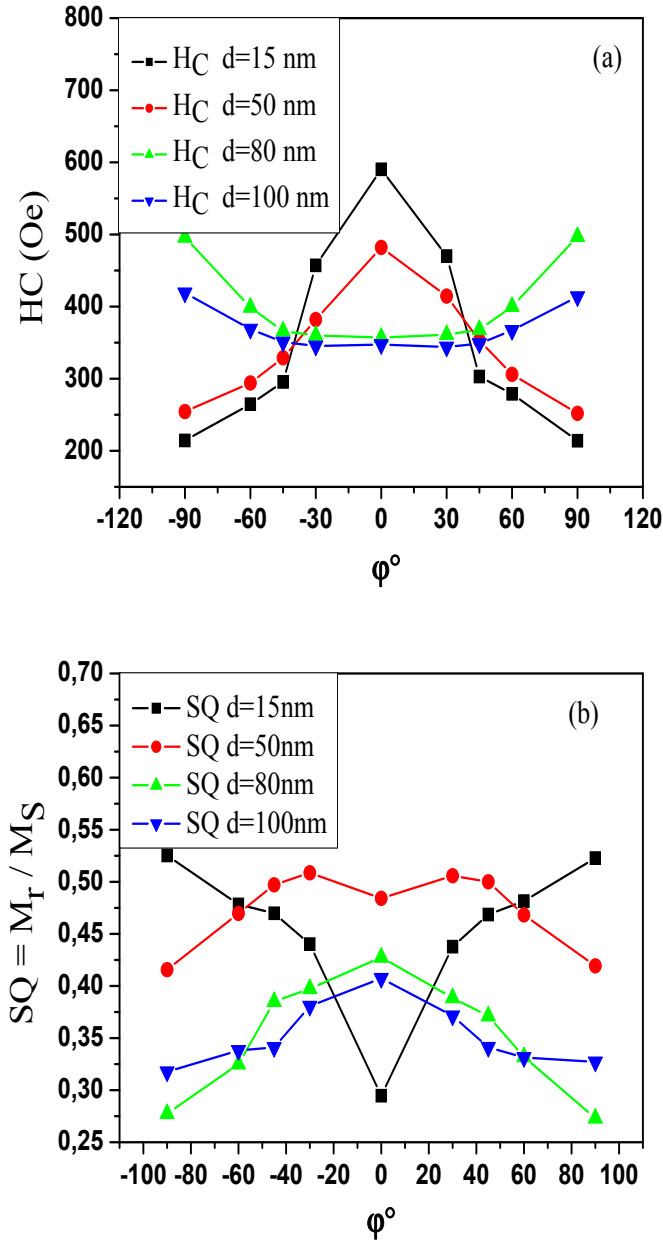


FIG. 7: Angular dependence of the coercivity  $H_C(\varphi)$  (a) and the squareness  $SQ$  (b) of nanowires in PCTE membranes with different diameters: 15, 50, 80 and 100 nm and  $6\mu\text{m}$  length.

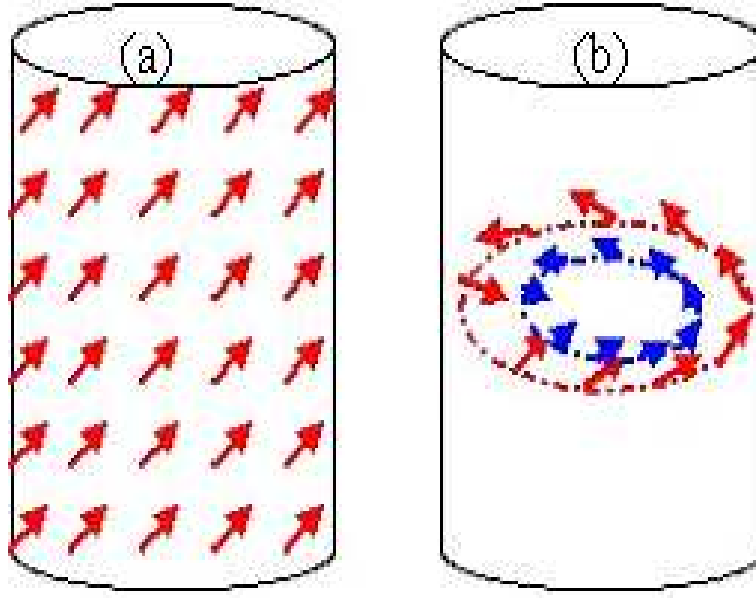


FIG. 8: Illustration of magnetization reversal in a single-domain cylinder: (a) coherent rotation and (b) curling case.

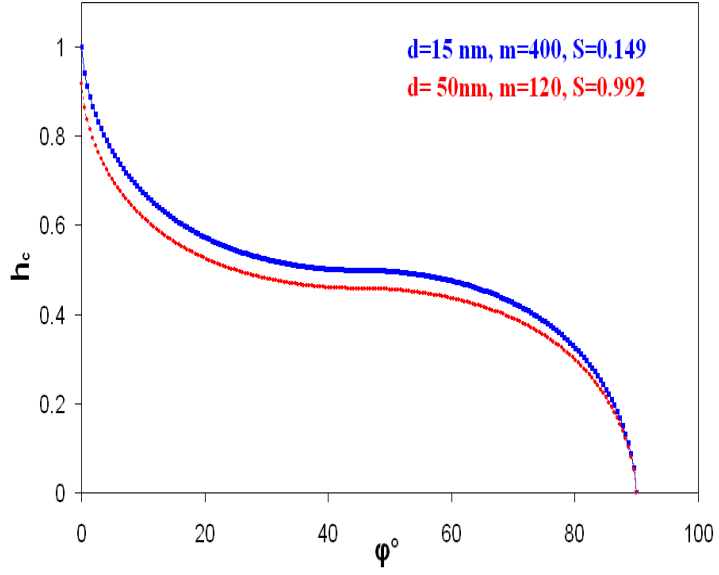


FIG. 9: Angular dependence of the reduced coercivity,  $h_C = \frac{H_C}{2\pi M_S}$ , in Stoner Wolhfarth case, where  $\varphi$  is the angle between the external applied field and the wire axis,  $d$  is the wire diameter,  $m = \frac{c}{a}$  is the aspect ratio and  $S = \frac{R}{R_0}$  is the reduced ratio.

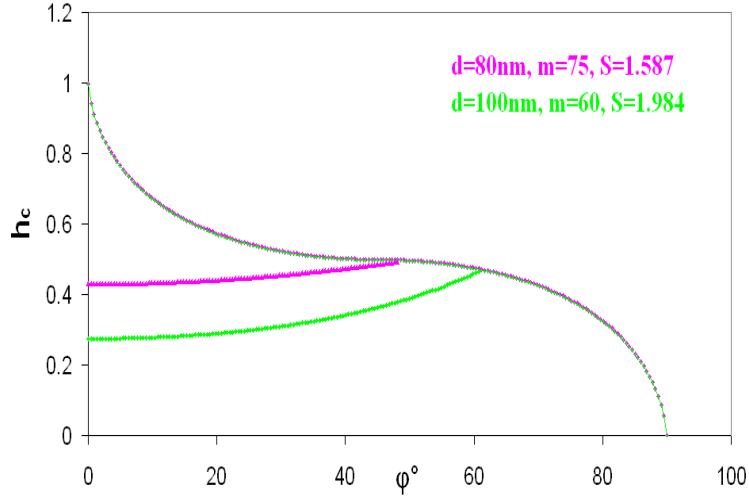


FIG. 10: Angular dependence of the reduced coercivity,  $h_C = \frac{H_C}{2\pi M_S}$ , in the Curling case, where  $\varphi$  is the angle between the external applied field and the wire axis,  $d$  is the wire diameter,  $m = \frac{c}{a}$  is the aspect ratio and  $S = \frac{R}{R_0}$  is the reduced ratio.



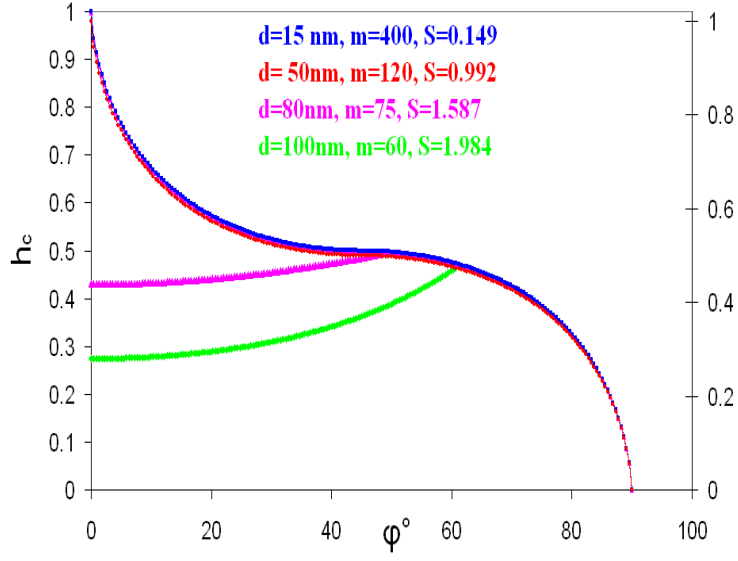


FIG. 11: Reduced coercivity  $h_c$  for aligned array of infinitely long single-domain cylindrical nanowires as function of angle  $\varphi$  between easy axis (i.e. cylindrical axis) and direction of measurement, where  $\varphi$  is the angle between the external applied field and the wire axis,  $d$  is the wire diameter,  $m = \frac{c}{a}$  is the aspect ratio and  $S = \frac{R}{R_0}$  is the reduced ratio.

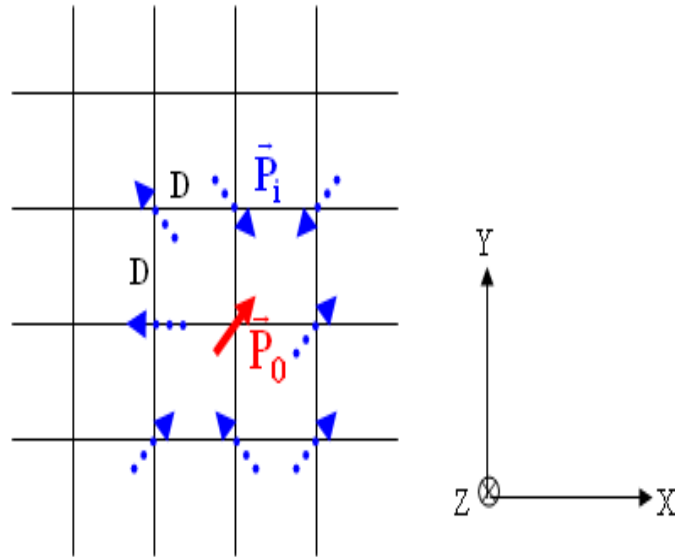


FIG. 12: Dipole  $\vec{P}_0$  surrounded by a number of  $\vec{P}_i$  dipoles sitting on a  $2D$  square lattice with  $D$  the average dipole separation.